Journal of Alloys and Compounds 490 (2010) 472–479

Contents lists available at ScienceDirect

Journal of Alloys and Compounds

journal homepage: www.elsevier.com/locate/jallcom

Texture, mechanical and thermoelectric properties of $Ca_3Co_4O_9$ ceramics

Driss Kenfaui*, Daniel Chateigner, Moussa Gomina, Jacques Guillaume Noudem

CRISMAT, UMR 6508 CNRS/ENSICAEN et Université de Caen Basse-Normandie, 6 Boulevard Maréchal Juin, 14050 CAEN Cedex 04, France

ARTICLE INFO

Article history:
Received 13 August 2009
Received in revised form 7 October 2009
Accepted 7 October 2009
Available online 17 October 2009

Keywords:
$Ca_3Co_4O_9$ ceramics
Hot-pressing
Spark plasma sintering
Texture
Mechanical proprieties
Thermoelectric proprieties

ABSTRACT

$Ca_3Co_4O_9$ thermoelectric (TE) ceramics have been processed using conventional sintering (CS), hot-pressing (HP) and spark plasma sintering (SPS). Microstructure investigations have revealed that HP processing is effective for obtaining highly textured 349 ceramics, with a degree of crystallite orientation showing a texture index of 6 mrd^2, and that SPS affords strong densified 349 ceramics, typically 98% of the theoretical X-ray density. Investigations of mechanical and thermal properties were undertaken for a reliable integration of these materials in practical devices. In detail, these properties were assessed by microindentation, nanoindentation and three point bending tests. Hardness, elastic modulus, strength and fracture toughness of the HP and SPS samples were drastically improved, compared with the CS specimen. The thermal expansions were measured and shown, for the samples processed by HP and SPS, different between the directions parallel and perpendicular to the stress axis. Thermoelectric properties were investigated from 5 to 850 K and a remarkable power factor value of 550 $\mu W\,m^{-1}\,K^{-2}$ was obtained at 850 K. Mechanical and TE properties were correlated to the microstructure and texture features.

1. Introduction

Since $NaCo_2O_4$ has been reported [1] to exhibit thermoelectric (TE) performance almost comparable to that of conventional semiconducting materials, increasing attention has been attached to other layered cobalt oxides having natural merits of low thermal conductivity and high oxidation resistance in air at high temperature. Some compounds like Bi–Ca/Sr–Co–O and Bi–Pb–Sr–Co–O [2–6] with enhancement of the figure-of-merit $ZT = S^2 \times T/\rho \times \kappa$ (S is the Seebeck coefficient, T the absolute temperature, ρ the electrical resistivity and κ the thermal conductivity) have been reported as promising TE materials. Owing to the volatility of Bi, Pb and Na at high temperature and their relatively high toxicity, the practical applications of the compounds indicated above are limited. In 1999, $Ca_3Co_4O_9$ (349), with high chemical and thermal stabilities, has been found [7] to exhibit a large thermopower. This compound is a misfit-layered oxide [8] consisting of two monoclinic subsystems, which are Ca_2CoO_3 and CoO_2 layers. Single crystals with a 349 structure have along the ab-planes, a figure-of-merit of 0.87 at 973 K in air [9]. However, the size of a 349 single crystal is too small for a practical use as in devices. An alternative way is to use polycrystalline materials by optimising their elaboration process. Hot-pressing (HP) and spark plasma sintering (SPS) processings have been reported [10,11] to allow elaboration of 349 ceramics with high textures and/or strong bulk density, both improving significantly their TE performances.

Basically, the 349 ceramics are reported as a potential hole-doped material for TE generators [7]. A typical application is the conversion of exhaust heat from automobiles and plants into electrical current.

But until now, the investigations of the mechanical properties of bulk 349 ceramics have been neglected and attention was mainly focused on the search for material synthesis, processing, resolution of the crystallographic structure and/or for thermoelectric properties. Knowledge of the thermal and mechanical properties is essential for the reliability of 349 ceramics in devices with small dimensions (few centimetres).

In this work, we synthesized a $Ca_3Co_4O_9$ powder using a solid-state reaction. The $Ca_3Co_4O_9$ bulk thermoelectric oxides were prepared using three different ways as: (i) conventional sintering (CS), (ii) hot-pressing (HP) and (iii) spark plasma sintering (SPS) method. The microstructures of the CS, HP and SPS samples are investigated and correlated to the elaboration parameters. The mechanical and TE properties are measured and correlated to the microstructure and texture features.

2. Experimental procedure

2.1. Sample preparation

$Ca_3Co_4O_9$ (349) powder was synthesized by a conventional solid-state reaction method. The starting precursors $CaCO_3$ and Co_3O_4 were thoroughly mixed in stoichiometric ratios for 30 min. The mixture was calcinated at 900 °C during 24 h in air, then ground and cold-pressed uniaxially (92 MPa) into pellets (25 mm in diameter).

* Corresponding author. Tel.: +33 231 45 13 15; fax: +33 231 45 13 09.
E-mail address: driss.kenfaui@ensicaen.fr (D. Kenfaui).

0925-8388/$ – see front matter © 2009 Elsevier B.V. All rights reserved.
doi:10.1016/j.jallcom.2009.10.048

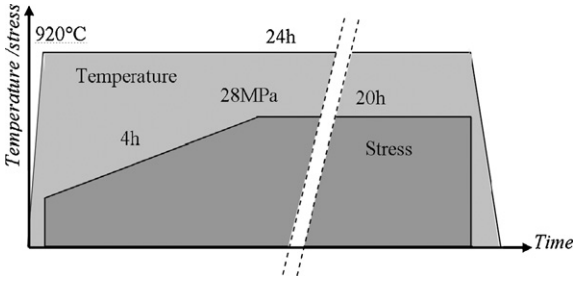

Fig. 1. Temperature and stress profiles as a function of time applied on the pellets during the HP processing.

The 349 ceramics were processed using three techniques: (i) conventional sintering, (ii) hot-pressing and (iii) spark plasma sintering. For the CS processing, the pellet was sintered at 920 °C for 24 h without any applied stress. In the case of the HP technique, the samples were processed using a home made hot-pressing furnace described elsewhere [12], by applying a thermo-mechanical cycle illustrated in Fig. 1. A uniaxial pressure of 28 MPa was applied for the dwell time at high temperature and removed before cooling in order to avoid microcracking of the sample. The maximum temperature during the heat treatment is 920 °C, which is 6 °C lower than the decomposition temperature [13] of the $Ca_3Co_4O_9$ phase.

Before SPS processing, the 349 powder was firstly uniaxial cold-pressed at 60 MPa into cylindrical pellets (13 mm in diameter) and then conventionally sintered at 920 °C for 24 h. The pre-sintered pellets were then placed in a graphite die with a diameter of 20 mm allowing a free lateral deformation of the samples. They were finally consolidated in the SPS device (Dr. Sinter 2080 Syntex machine) at the "*Plate-forme Nationale de Frittage Flash, CNRS, Toulouse, France*". The pulsed electric current (2000 A, 4 V) was passed through the sample to heat it up to the dwell temperature (750 °C) while a uniaxial pressure of 50 MPa was applied for 2 min under vacuum (10^{-3} bar). The as-prepared sample was moderately heated and polished to remove the graphite foil used during processing before undergoing further characterizations.

2.2. Microstructure and texture

The microstructures of 349 ceramics were examined by using a Carl Zeiss (Supra 55, Oberkochen, Germany) scanning electron microscope (SEM). The phase composition and the texture of the samples were investigated by using X-ray diffraction on a 4-circle diffractometer set-up equipped with a curved position sensitive detector (CPS120 from INEL SA), and operating with a monochromatised Kα-Cu radiation, as described in details elsewhere [14], and within the combined analysis formalism [15] implemented in MAUD [16]. Briefly, this methodology allows the quantitative texture determination of the samples, using a cyclic Rietveld refinement of a series of X-ray diagrams recorded at different sample orientations. Due to the expected texture strength in such materials and the axially symmetric texture (induced by the deformation under uniaxial pressing stress), we measured 13 diagrams every 5° in tilt angle χ, for an incident angle of the X-ray beam on the sample of $\omega = 20°$. The instrument contributions (χ and ω broadenings, peak shapes, zero-shifts) were calibrated using the LaB_6 powder standard from the NIST. A counting time of 10 min for each sample orientation was used, and our optical set-up provides with a 0.1° peak widths in 2θ. Pole figures obtained here are normalised into multiples of a random distribution (mrd), a unit that does not depend on other factors than orientation. In such units, a sample without preferred orientations exhibits uniform pole figures with 1 mrd levels, while a textured sample shows pole figures with maxima and minima of orientation densities ranging from 0 mrd (absence of crystals oriented in this direction) to infinity (for a single crystal on few directions). The overall texture strength is evaluated through the texture index [17] which is expressed in mrd^2 units and varies from 1 (random powder) to infinity (perfect texture or single crystal). This index is used to compare the texture strength of different samples exhibiting similar orientation distributions (OD). Such normalised pole figures are calculated from the OD of crystallites, refined using the E-WIMV formalism [18] after extraction of the peak intensities during the Rietveld cycles. The OD and profile refinement reliabilities are estimated using conventional reliability factors [19]. During these refinements we used the supercell definition of 349 as previously [20].

2.3. Mechanical tests

To determine the microhardness, μH, of the 349 ceramics, a course of microindentation tests at room temperature was carried out via Vickers indentation on polished surfaces of the samples using a Zwick mechanical testing machine. For the samples elaborated by HP and SPS, the direction of load application by the indenter was parallel to the pressing axis during the sintering process. All the microindentation tests were performed with a loading time of 15 s and the microhardness, μH, was calculated from the applied load, P, and the diagonal lengths, d_1 and d_2, of the indentation impression such that [21]:

$$\mu H = \frac{1.8544 \times P}{(d_1 \times d_2)} \quad (1)$$

Nanoindentation tests were performed on the samples by using a Nano Indenter® XP (MTS Systems Corporation, Eden Prairie, MN, USA) equipped with a Berkovich tip. The maximum penetration depth was chosen to be 5000 nm for the CS samples and 2000 nm for the HP and SPS samples. For each test, nine impressions, arranged in a 3×3 array, were introduced on the polished sections with 50 μm spacing to minimize the possible interaction between the deformed areas. After the indentation load was removed, the load-displacement data were used to calculate nanohardness, nH, and elastic modulus, E.

The nanohardness, nH, of a sample can be calculated from the following equation:

$$nH = \frac{P}{A} \quad (2)$$

where P refers to the load measured at the penetration depth, h, while A refers to the projected contact area between the indenter and the sample.

The elastic modulus of the tested sample, E, is determined from the reduced modulus, E_r, given by:

$$E_r = \frac{\sqrt{\pi} \times S}{2 \times \beta \times \sqrt{A}} \quad (3)$$

where $S = dP/dh$ is the elastic stiffness of the contact. β is a factor that depends only on the geometry of the indenter, $\beta = 1.034$ for Berkovich tip. The modulus, E, can then be calculated as follows:

$$E = \frac{(1 - \nu^2)}{1/E_r - (1 - \nu_i^2)/E_i} \quad (4)$$

where ν and ν_i are the Poisson's ratios of the specimen and indenter, respectively, while E_i is the elastic modulus of the indenter. All these formula are established for the isotropic case, corresponding to the CS sample, but with deviations particularly for HP, and to a much lesser extent for SPS, which are neglected in this work.

In our experiments, the nanohardness and Young's modulus were not derived from the initial unloading curve as advocated by Oliver and Pharr [22]. We made use of the continuous stiffness measurements (CSM) option of the Nano Indenter® XP, which allowed the evaluation of the elastic contact stiffness S all along the loading path of the load-penetration curve.

The strength (fracture stress), σ_R, was determined for our 349 ceramics at room temperature by three point bending tests. The HP sample was too thin to be tested by using this technique. To get a thick HP sample, we have welded together a stack of five thin samples by hot-pressing at 920 °C under 10 MPa for 5 h. SEM observations revealed that the thin HP samples were well welded between each others and no noticeable deterioration of the structure or the texture had occurred after the hot-stacking treatment. Bars for mechanical tests were cut from the samples, with $w \sim 2$ mm thickness, $B \sim 3$ mm width and $L = 12$ mm span. The load was applied in the direction parallel to the pressing axis for the HP and SPS samples.

Fracture toughness measurements were performed on SENB specimens with relative notch length of $a_o/w \sim 0.33$ introduced by using a 50 μm thick saw.

2.4. Thermal measurements

Thermal expansion was assessed in the temperature range 50–900 °C. For the HP and SPS samples, these measurements were carried out in two directions: parallel and perpendicular to the pressing stress axis (out-of-plane and in-plane, respectively).

2.5. Thermoelectrical measurements

Bar-shaped samples 12 mm long, 2 mm width and 0.4–2 mm thick for electrical characterization were cut into the processed pellets by using a low speed diamond saw (Struers, Champigny sur Marne, France). The temperature dependence of electrical resistivity, ρ, was measured by the standard DC four-probe method by mean of a Quantum Design Physical Property Measurement System (PPMS, Oxford, Inc., UK) from 5 K to room temperature. The high temperature (from room temperature to 850 K) electrical resistivity and Seebeck coefficient measurements were simultaneously performed by using ZEM-3 (ULVAC-RIKO, Inc., Japan) apparatus.

3. Results and discussion

3.1. Microstructure and texture

SEM micrographs of the surfaces of rupture of CS, HP, and SPS samples (Fig. 2) were performed on the planes containing the pressing axis as indicated by the arrow in Fig. 2b and c. As shown from Fig. 2a, the microstructure of the CS sample exhibits small grains

with typical sizes less than 5 μm, which appear to be randomly oriented. One also observes a large number of pores which greatly reduces the bulk density and may impair the mechanical and thermoelectrical properties. In the HP sample (Fig. 2b), we observe clearly a strong alignment of large platelets homogenously distributed and compactly stacked up along the pressing axis. Indeed, for a pressure level of 28 MPa, the grains turn into platelets and their lateral size increases from about 5 to about 17 μm, while their thickness does not exceed 0.15 μm. Thus, much of the porosity is removed, which improves significantly the bulk density. In the case of the SPS processed sample (Fig. 2c), a fairly high bulk density is obtained for a pressure level of 50 MPa and no preferential grain orientation is observed after a quick processing of 2 min. The platelets in-plane dimensions were slightly increased (≤8 μm). As measured from sample mass and volume determinations, the bulk density of the CS, HP and SPS samples are 2.82, 4.45 and 4.59 g/cm^3, which corresponds to 60%, 95% and 98% of the theoretical density [8], respectively.

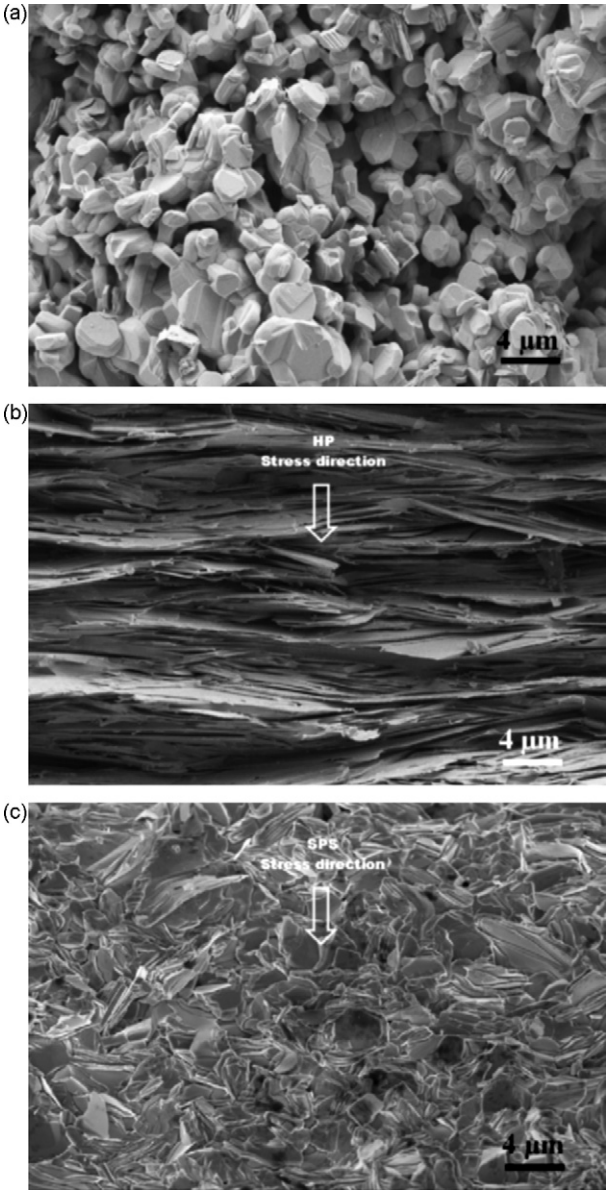

Fig. 2. SEM micrographs of fractured surfaces of the $Ca_3Co_4O_9$ samples processed by: (a) conventional sintering (CS), (b) hot-pressing (HP) and (c) spark plasma sintering (SPS) processings.

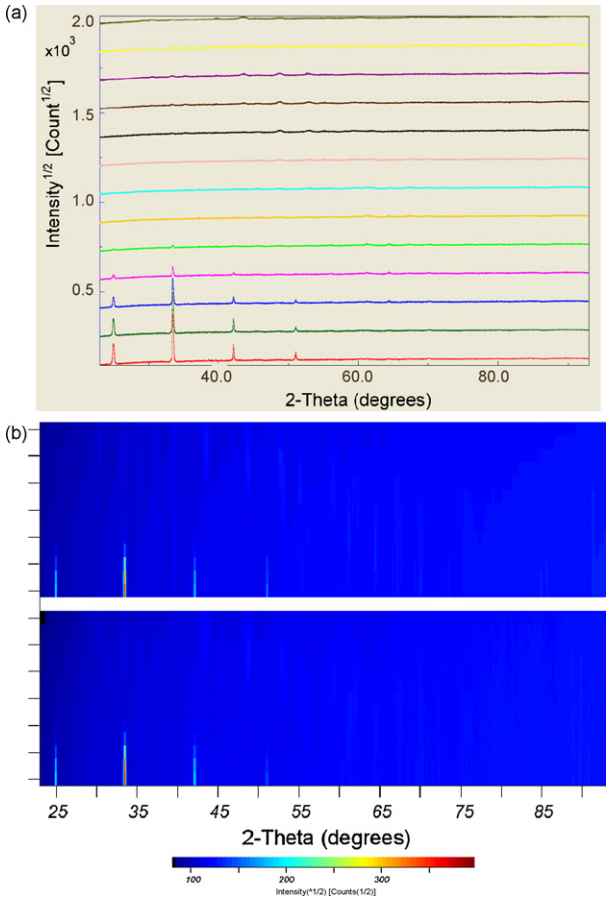

Fig. 3. HP sample X-ray diagrams (a) χ-evolution of the diffracted diagrams. χ goes from 0 (bottom diagram) to 60° (top diagram) by steps of 5°, and (b) experimental (bottom) and refined (top) series of diagrams.

While the CS sample exhibits no crystallographic texture, results from the combined analysis of the HP sample (Fig. 3a) reveal a strong decrease of the 0 0 ℓ lines of the 349 structure with the tilt angle, as an indication of a strong texture. After refinement, the calculated diagrams compare well with the experiments (Fig. 3b), within reliability factors as low as $Rw = 3.26\%$, $R_{Bragg} = 2.27\%$, $R_{expected} = 0.85\%$, giving a goodness of fit of GoF = 3.81. The resulting cell parameters after refinement are $a = 4.8573(3)$ Å, $b = 36.526(3)$ Å, $c = 10.8547(3)$ Å, $\beta = 97.913(3)°$, coherent with the usual bulk values for this phase, and a mean isotropic crystallite size of 654(45) nm, in accordance with the mean dimension of the grains as revealed by SEM. This latter point testifies for the HP processing to afford strongly oriented grains.

The combined OD refinement allows the reconstruction of the {0 2 0}, {0 0 1} and {1 0 0} pole figures (Fig. 4a). This refinement was obtained with reliability factors of the OD of $Rw = 1.29\%$ and $R_{Bragg} = 2.67\%$, which are very low values for such a high texture strength having $F^2 = 6$ mrd^2. The pole figures clearly show that the ⟨0 0 1⟩ directions (normal to the {0 0 1} planes) are strongly aligned parallel to the stress axis (centre of the pole figures), with a maximum of the {0 0 1} poles of around 22 mrd, the largest value obtained to date on 349 ceramics. The maximum value of the OD is 118 mrd, and its minimum is 0, indicating that all the crystallites are oriented within the fibre orientation components. The inverse pole figure calculated for the pressure axis indicates that no other significant orientation component than the fibre ⟨0 0 1⟩ exists (Fig. 4b) and corresponds to levels of orientation along the pressure axis up to 57 mrd.

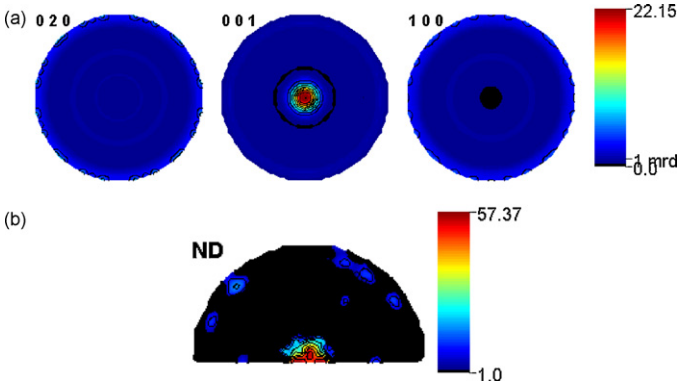

Fig. 4. (a) {0 2 0}, {0 0 1} and {1 0 0} pole figures for the HP sample obtained after OD refinement (linear density scale, equal area projection) and (b) inverse pole figure calculated for the direction of the pressure (logarithmic density scale and equal area projection).

The SPS sample quantitative texture analysis indicates a lower crystallographic texture strength. The {0 2 0}, {0 0 1} and {1 0 0} pole figures (Fig. 5a) of this sample culminate at 3.8 mrd at the centre of {0 0 1}, quite 6 times lower than for HP. Also, small ⟨100⟩ orientation components exist in this sample, as visible in the inverse pole figure (Fig. 5b).

Although the Rietveld refinement was obtained with less reliability ($Rw = 8.55\%$, $R_{Bragg} = 4.19\%$, $R_{expected} = 1.30\%$, GoF = 6.59) and poorer cell parameters ($a = 4.741(2)$ Å, $b = 36.44(2)$ Å, $c = 10.854(1)$ Å, $\beta = 98.21(3)^\circ$, the OD refinement is still good ($Rw = 4.26\%$ and $R_{Bragg} = 3.42\%$). These relatively poorer reliabilities are mainly due to the presence of still unidentified peaks. The mean isotropic coherent domain size is much lower than for HP 100(15) nm, which corroborates the lower mean dimension of the grains evidenced by SEM.

With a texture strength of $F^2 = 5$ mrd^2, a maximum value of the OD of 26 mrd (still a minimum of 0), and an inverse pole figure maximum of 7 mrd, one clearly notes a strong texture decrease compared to the HP sample.

3.2. Mechanical properties

3.2.1. Microindentation

The average values of Vickers microhardness obtained for the CS, HP and SPS samples are summarized in Table 1. The CS sample was tested under $P = 2$ N load, while the HP and SPS samples under 5 and 15 N, respectively. The load was applied parallel to

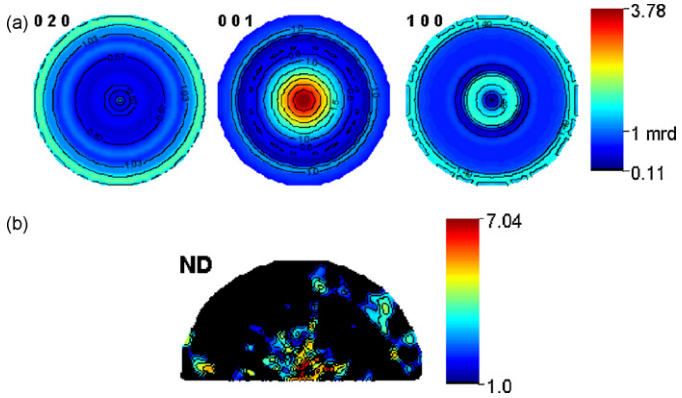

Fig. 5. (a) {0 2 0}, {0 0 1} and {1 0 0} pole figures for the SPS sample obtained after OD refinement (linear density scale, equal area projection) and (b) inverse pole figure calculated for the direction of the pressure (logarithmic density scale and equal area projection).

Table 1
Average microhardness obtained via Vickers indentation for CS, HP and SPS samples.

Processing	CS	HP	SPS
Microhardness, μH (GPa)	0.12 ± 0.01	1.31 ± 0.12	1.55 ± 0.09

HP and SPS pressing axis and results then in a partially anisotropic loading scheme. The microhardness, μH, rises from 0.12 ± 0.01 GPa for the CS sample to 1.31 ± 0.12 GPa for the HP sample. μH is then about 11 times larger when the bulk density increases from 60 to 95% as a consequence of the hot-pressing effect. The microhardness of the SPS sample is even more improved (13 times): it increases to 1.55 ± 0.09 GPa although the grain size and the texture strength were not significantly increased. The microhardness difference between HP and SPS is then due essentially to the stronger densification for the SPS sample (98%), since the texture has decreased between HP and SPS. Thus, the increase in Vickers microhardness values can be correlated to both the strong densification and texture increase from CS to HP, and mainly due to further densification of 349 from HP to SPS processing. Also, the signature of the good alignment between the platelets (morphological texture) on the microhardness increase between CS and HP seems to be influent, while negligible between CS and SPS.

It should be noticed that the microhardness obtained here for the 349 ceramics processed using HP and SPS is 2.1 and 2.5 times, respectively, larger than that reported for the conventional materials Bi_2Te_3 [23], frequently integrated in TE modules for energy conversion applications.

In contrast of the majority of brittle materials, e.g. superconductors [24], Vickers indentation of the CS, HP and SPS materials did not lead to cracking around the indent impression. Then, we could not determine their fracture toughness by measuring crack lengths.

3.2.2. Nanoindentation

Nanoindentation tests were carried out for all the samples with the aim to determine the Young's modulus and to compare nanohardness versus microhardness values. First of all, the HP pellet was cut to eliminate the weakest densified zones. Then, five areas of the CS, HP (Fig. 6a) and SPS samples were chosen for the nanoindentation test. For each area, a batch of nine impressions was selected. As an example, the pattern of residual impressions, left after the Berkovich indenter was withdrawn, is shown on the micrograph of Fig. 6b.

In the nanoindentation test, the applied load P is continuously measured versus the indenter displacement, h. The load-displacement curve is obtained from a complete loading-unloading cycle (Fig. 6c as an example for area number 2). The derived nanohardness-displacement and the Young's modulus-displacement curves are illustrated in Fig. 6d. The average nanohardness and Young's modulus values calculated for each areas of the HP sample are given in Table 2. The average nanohardness, nH, value of the HP sample is 2.08 ± 0.15 GPa.

Fig. 7a shows the nanohardness, nH, and Young's modulus, E, values obtained for CS, HP and SPS samples. The nanohardness value (2.59 ± 0.10 GPa) of the SPS sample (most densified and weakly textured) is larger than that of the HP sample. Both SPS and HP samples exhibit nH considerably improved in comparison with CS sample (0.11 ± 0.03 GPa). However, nH and μH values seem to record a different increase for HP and SPS specimens. While the CS sample exhibits μH and nH of around 0.11 GPa, the increase factor in hardness from HP to SPS is 1.18 for μH and 1.25 for nH measurements. Taking into account the error values, these ratios are quite the same.

Young's modulus, E, was derived by assuming an isotropic model even in the case of HP samples. For this sample (strongly

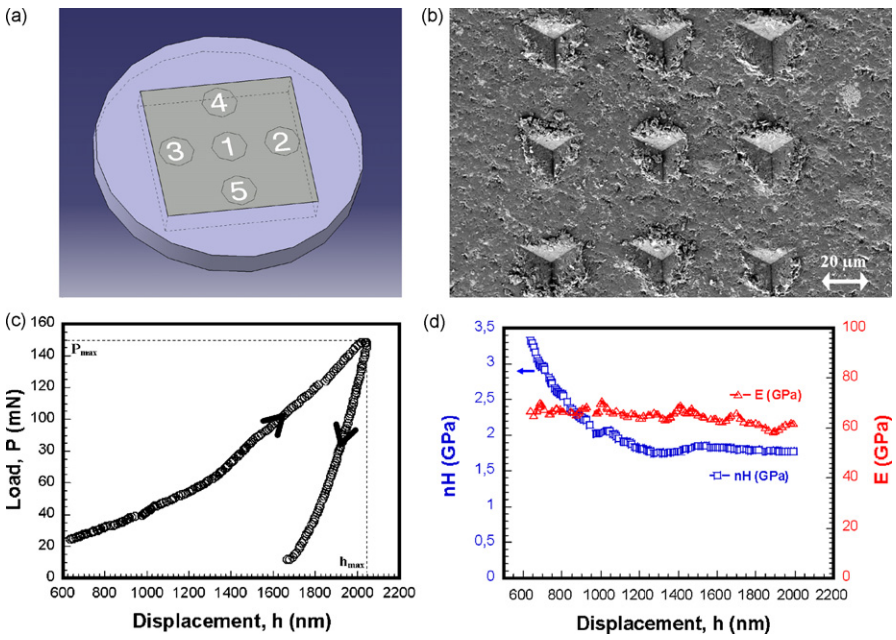

Fig. 6. (a) Five areas of HP sample tested by nanoindentation, (b) A 3 × 3 matrix pattern of residual impressions introduced on area number 2 of HP sample, (c) load–displacement curve obtained for the nanoindentation of area number 2 and (d) hardness and Young's modulus vs displacement for area number 2.

Table 2
Average nanohardness and Young's modulus values obtained via nanoindentation technique for each area of the HP sample.

Area	1	2	3	4	5
Nanohardness, *nH* (GPa)	2.08 ± 0.31	2.05 ± 0.26	2.04 ± 0.41	2.09 ± 0.32	2.13 ± 0.50
Young's modulus, *E* (GPa)	45.31 ± 2.00	56.92 ± 3.46	60.97 ± 4.50	52.95 ± 3.51	62.84 ± 4.85

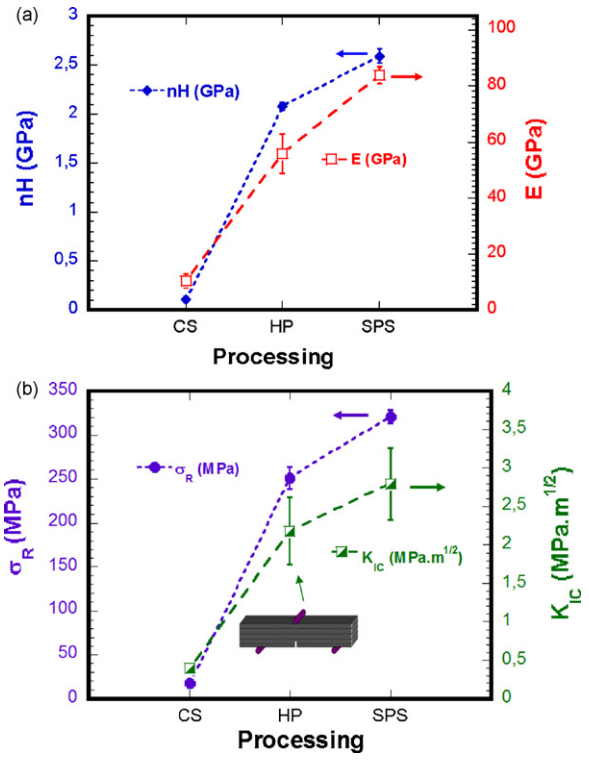

Fig. 7. (a) Nanohardness, Young's modulus and (b) fracture stress and toughness values obtained for samples elaborated by CS, HP and SPS processing.

anisotropic), the derivation of the Young modulus is biased since the load is applied parallel to the mean *c*-axes direction which, due to the indenter shape, transfers in an inclined manner to the sample hereby probing preferentially specific c_{ij} stiffness constants. This is not the case of the two other lowly textured samples probed in the same way. One observes the processing influence on *E* is similar to that on Hardness: the SPS sample exhibits the largest *E* value (84 ± 3 GPa), which is 8 fold the *E* value of the CS sample (10.5 ± 2.5 GPa). The elastic modulus of the HP sample (strongly textured) is 56 ± 7 GPa, i.e. 5 times the CS value.

Furthermore, the 349 materials consolidated by HP and SPS exhibited elastic modulus values that are 1.7 and 2.6 times, respectively, higher than that reported for Bi_2Te_3 ones [23].

3.2.3. *Fracture stress and toughness*

Like the Young's modulus and hardness, the fracture stress, σ_R, values depend on the processing method [31] (Fig. 7b). The results point out the effectiveness of HP and SPS to ameliorate the strength of 349 TE ceramics. An improvement in σ_R by a factor of about 14 is recorded for HP sample compared to the CS one, while the factor for SPS specimen is close to 18. That is an illustration of the higher bulk density provided by the SPS processing.

Regarding the fracture toughness, K_{IC} (Fig. 7b), it appears that SPS is more effective for increasing the reliability of 349 ceramics by enhancing their resistance to the spreading of major flaw. K_{IC} value as high as 2.8 ± 0.47 MPa $m^{1/2}$ is obtained for the SPS specimen, corresponding to an improvement factor of more than 7, in comparison with the CS sample (0.4 ± 0.02 MPa $m^{1/2}$). The improvement factor of 349 ceramics processed by HP (2.2 ± 0.43 MPa $m^{1/2}$) exceeds 5, but it is still lower than that of the SPS. SEM observations revealed that fracture proceeds by crack deflection by the platelets and breaking of the grain boundaries.

We can finally conclude the increase in the mechanical properties is more related to the densification of the 349 ceramics than to their texture strength.

Poor mechanical properties have been reported for Bi_2Te_3 single crystals and even polycrystals [25]. In the case of our HP 349 ceramics, one could expect similar behaviours but suffer any experimental data because no large enough crystals could be grown to carry out the corresponding mechanical measurements. But, in our 349 polycrystalline textured materials (HP samples), Vickers hardness values, Young's modulus, fracture stress and toughness are 2.1, 1.7, 2 and 2 times, respectively, larger than the ones of Bi_2Te_3 polycrystalline textured samples [23,25]. In such a way, the HP 349 ceramics elaborated in the present work can be considered as less suffering cleavage effects than Bi_2Te_3 single crystals or polycrystals.

On the other hand, the fracture stress and toughness obtained for our SPS samples are 2.7 and 2.4, respectively, larger than those of the Bi_2Te_3 polycrystalline materials [23,25].

Thus the good mechanical properties of the 349 TE materials provide sufficient ability for their reliable integration and operating in TE modules.

3.3. Thermal analysis

Fig. 8 represents the thermal expansion behaviour in the temperature range 50–900 °C for the CS sample and, in the directions parallel and perpendicular to the pressing stress (out-of-plane and in-plane, respectively), for the HP and SPS specimens. These analyses were made on the thick hot-stacked sample for the ceramics processed by HP. It is clearly observed a noticeable difference in the thermal behaviour along the heating and the cooling paths, except along the mean in-planes of the HP specimen in the 550–900 °C temperature range. Such difference may be explained by the effects of irreversible phenomena occurring at the grain boundaries. One also sees a large difference in thermal behaviour for both directions. While the coefficient of thermal expansion (CTE) of the CS sample is $\alpha_{CS} = 12.6 \times 10^{-6}\,K^{-1}$, those of the HP sample evaluated in out-of-plane and in-plane are $\alpha^{c}_{HP} = 15 \times 10^{-6}\,K^{-1}$ and $\alpha^{ab}_{HP} = 7.3 \times 10^{-6}\,K^{-1}$, respectively. The obtained CTE ranking ($\alpha^{ab}_{HP} < \alpha_{CS} < \alpha^{c}_{HP}$) associated with the CTE ratio $\alpha^{c}_{HP}/\alpha^{ab}_{HP} \approx 1.73$ reveals the influence of the grain boundary density and the strong platelets alignment as a result of a particular effect of the HP processing. The SPS specimen exhibited an equivalent in-plane CTE ($\alpha^{ab}_{SPS} = 8 \times 10^{-6}\,K^{-1}$), due to a better connection between the platelets (densification effect) which compensated the weakness in the sample texture strength. But, its out-of-plane thermal behaviour displayed larger CTE value ($\alpha^{c}_{SPS} = 18.8 \times 10^{-6}\,K^{-1}$). That may be related to two different factors: the very low texture strength and to the larger out-of-plane grain boundary density. Hence, its CTE ratio is higher ($\alpha^{c}_{SPS}/\alpha^{ab}_{SPS} = 2.35$).

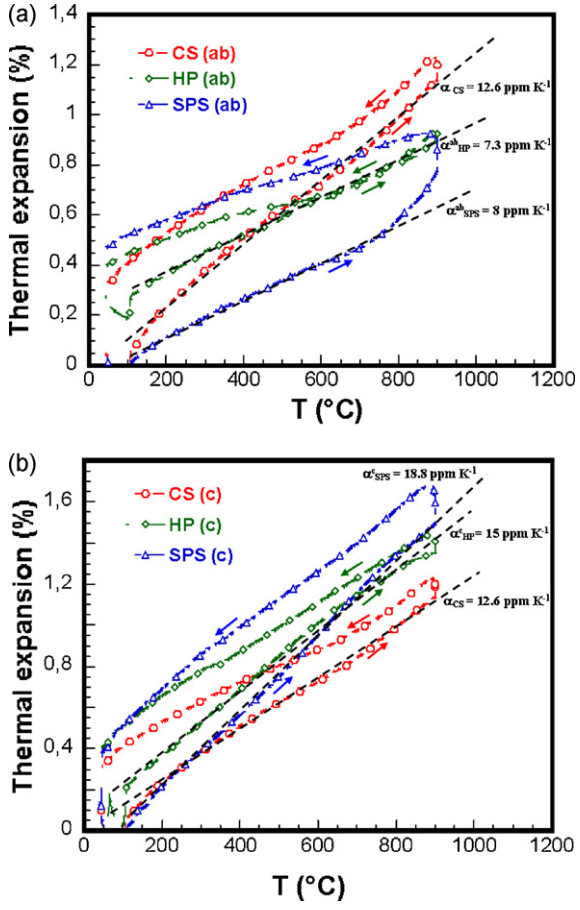

Fig. 8. Thermal analysis of the CS sample and in **(a)** in-plane and **(b)** out-of- plane (ab and c, respectively) for the HP and SPS samples.

These results indicate that the microstructure anisotropy and texture induced by the HP and SPS processings generate a strong anisotropy in the thermal behaviour of the 349 ceramics.

On the other hand, the in-plane CTE evaluated for the HP and SPS ceramics are close to some oxide materials (e.g. alumina: $8 \times 10^{-6}\,K^{-1}$). Their out-of-plane CTE are similar to those of metals (e.g. copper: $16 \times 10^{-6}\,K^{-1}$ and silver: $19\,K^{-1}$, respectively). As a consequence, both strongly densified and highly textured 349 ceramics can be connected to others materials for electrical (e.g. silver and/or copper metals) and thermal contacts (e.g. Al_2O_3 plate) in TE modules, with a good reliability and significantly improved efficiency.

3.4. Thermoelectrical properties

Fig. 9a shows the temperature ($5 \leq T \leq 350\,K$) dependence of the electrical resistivity, ρ, for the three 349 samples. The ρ (T) curves of the CS, HP and SPS samples show a similar behaviour, corresponding to the metal to semiconducting transition from room temperature to 5 K. This is in agreement with earlier reports [8,26–28] on these thermoelectric oxides. For the HP and SPS samples, the current was injected perpendicular to the pressing direction, i.e. the current flows along the mean in-planes (ab-planes) of the structure, particularly for HP strongly textured specimen. The comparison between the samples prepared by various methods shows clearly that the ρ values of HP and SPS specimens are much lower than the CS one. This can be explained as resulting from both densification and texture, but the texture is expected not to be the leading parameter, especially for the SPS sample. The good alignment between platelets also contributes to reduce the resistivity, which is more visible when comparing the HP and SPS resistivity curves, the former exhibiting lower ρ values than SPS above 50 K (Fig. 9a and b). The resistivity of the HP sample at 300 K, ρ_{300K}, is 6.1 mΩ cm which is among the best published values in the literature [5,29,30].

Fig. 9b shows the resistivity behaviour at high temperature for the three samples. The HP and SPS samples exhibit similar resistivity behaviour. But the resistivity of HP remains lower than that of SPS on the whole probed temperature range, resistivity values being at 800 K of 6 and 8 mΩ cm for HP and SPS, respectively. These values are, respectively, 7 and ~5 times lower than the resistivity of the CS sample for which 42 mΩ cm is measured at 800 K.

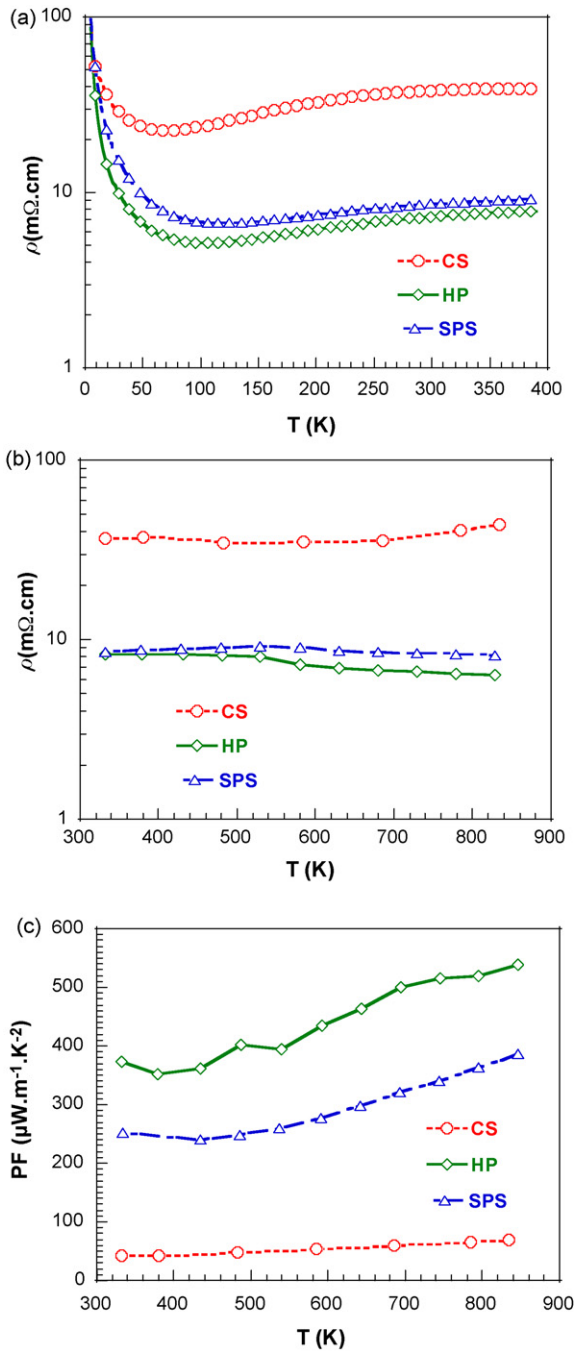

Fig. 9. Temperature dependence of electrical resistivity, ρ: (a) low temperature, (b) high temperature ranges and (c) temperature dependence of the power factor: $PF = S^2/\rho$.

All the samples processed in this work are from the same chemical composition. The Seebeck coefficient, S, values are then nearly similar for CS, HP and SPS samples, respectively. The positive ($S = 170\ \mu V\ K^{-1}$ at 800 K) value indicates that the majority of charge carriers are hole-like and the values measured on our 349 ceramics are consistent with data published in the literature [5,29,30].

Consequently, the power factor deduced from S and ρ values, $PF = S^2/\rho$, is significantly improved for the HP and the SPS samples, compared with the CS one (Fig. 9c). The PF reaches 550 $\mu W\ m^{-1}\ K^{-2}$ at 850 K for the HP 349 ceramics. This value is among the best published ones; it is larger than the reported values issued from 349 ceramics processed by SPS process [5,29], by combination of the magnetic alignment technique and SPS processing [5], or by HP [30].

4. Conclusion

$Ca_3Co_4O_9$ thermoelectric ceramics have been processed using conventional sintering, hot-pressing and spark plasma sintering techniques. The HP and SPS processings are efficient for obtaining highly textured and strongly densified $Ca_3Co_4O_9$ ceramics, respectively. As a result, the mechanical properties were distinctly enhanced. The microhardness of HP and SPS ceramics was about 11 and 13 times, respectively, larger than CS one. The nanoindentation technique confirmed these results and allowed to determine the elastic modulus which was more than 5 and 8 fold increased for HP and SPS samples, respectively, compared to the CS sample. Fracture stress of 349 ceramics consolidated by HP and SPS was drastically enhanced by factors of about 14 and 18, while the toughness was more than 5 and 7 fold improved, respectively. The thermal expansion shows different in-plane and out-of-plane values for both HP and SPS ceramics. The thermoelectric properties were also remarkably improved by HP and SPS processings. The power factor reaches 550 $\mu W\ m^{-1}\ K^{-2}$ at 850 K for the HP ceramics, among the best reported values.

The thermal expansion data and large mechanical investigations proposed, for the first time at our knowledge, positively influences the choice of such ceramic materials for their reliable integration as thermoelectric elements into modules.

Acknowledgements

D. Kenfaui and the authors acknowledge the “Conseil Régional de Basse Normandie, France” for its fellowship financial and financial participation for experimental set-up used in this work. The authors thank also Prof. J. Galy for his help during the SPS samples preparation and Mr. J. Lecourt during the 349 powders synthesis.

References

[1] I. Terasaki, Y. Sasago, K. Uchinokura, Phys. Rev. B. 56 (R12) (1997) 685–687.
[2] M. Hervieu, Ph. Boullay, C. Michel, A. Maignan, B. Raveau, J. Solid State Chem. 142 (1999) 305–318.
[3] G. Xu, R. Funahashi, M. Shikano, I. Matsubara, Y. Zhou, J. Appl. Phys. Lett. 91 (2002) 4344–4347.
[4] R. Funahashi, I. Matsubara, S. Sodeoka, Appl. Phys. Lett. 76 (2000) 2385–2387.
[5] Y. Zhou, I. Matsubara, S. Horii, T. Takeuchi, R. Funahashi, M. Shikano, J.I. Shimoyama, K. Kishio, W. Shin, N. Izu, N. Murayama, J. Appl. Phys. 93 (2003) 2653–2658.
[6] A. Maignan, S. Hebert, D. Pelloquin, C. Michel, J. Hejtmanek, J. Appl. Phys. 92 (2000) 1964–1967.
[7] S. Li, R. Funahashi, I. Matsubara, K. Ueno, H. Yamada, J. Mater. Chem. 9 (1999) 1659–1660.
[8] A.C. Masset, C. Michel, A. Maignan, M. Hervieu, O. Toulemonde, F. Studer, B. Raveau, Phys. Rev. B. 62 (2000) 166–175.
[9] M. Shikano, R. Funahashi, Appl. Phys. Lett. 82 (2003) 1851–1853.
[10] M. Prevel, B. Ouladdiaf, J.G. Noudem, S. Lemonnier, Y. Klein, S. Hébert, D. Chateigner, J. Appl. Phys. 98 (2005) 0937061–0937064.
[11] J.G. Noudem, M. Prevel, A. Veres, D. Chateigner, J. Galy, J. Electroceram. 22 (2009) 91–97.
[12] V. Rouessac, J. Wang, J. Provost, G. Desgardin, Physica C 268 (1996) 225–232.
[13] E. Woermann, A. Muan, J. Inorg. Nucl. Chem. 32 (1970) 1455–1459.
[14] J. Ricote, D. Chateigner, Bol. Soc. Esp. Ceram. Vidrio. 38 (1999) 587–591.
[15] D. Chateigner, Combined analysis: structure-texture-microstructure-phase-stresses-reflectivity analysis by X-ray and neutron scattering, (2004) 147, http://www.ecole.ensicaen.fr/~chateign/texture/combined.pdf.
[16] L. Lutterotti, S. Matthies, H.R. Wenk, in: J.A. Spunar (Ed.), MAUD (Material Analysis Using Diffraction): A User Friendly Java Program for Rietveld Texture Analysis and More, Texture of Materials: Proceeding of ICOTOM14, National Research Council of Canada, Ottawa, 1999, pp. 1599–1604.
[17] S. Matthies, G. Vinel, K. Helming, in: S. Matthies, G. Vinel, K. Helming (Eds.), Standard Distributions in Texture Analysis, vol. 1, Akademie-Verlag, Berlin, 1987, pp. 1–449.
[18] L. Lutterotti, D. Chateigner, S. Ferrari, J. Ricote, Thin Solid Films 450 (2004) 34–41.
[19] D Chateigner, J. Appl. Crystallogr. 38 (2005) 603–611.

[20] E. Guilmeau, D. Chateigner, J. Noudem, R. Funahashi, S. Horii, B. Ouladdiaf, J. Appl. Crystallogr. 38 (2005) 199–210.
[21] J.B. Wachtman, Mechanical Properties of Ceramics; Edited by Jr., Wiley and Sons, New York, INC., 1996.
[22] W.C. Oliver, G.M. Pharr, J. Mater. Res. 7 (1992) 1564–1583.
[23] L.-D. Zhao, B.-P. Zhang, J.-F. Li, M. Zhou, W.-S. Liu, J. Liu, Alloys Compd. 455 (2008) 259–264.
[24] F. Tancret, I. Monot, F. Osterstock, Mater. Sci. Eng. A. 298 (2001) 268–283.
[25] L.D. Zhao, B.-P. Zhang, J.-F. Li, H.L. Zhang, W.S. Liu, Solid State Sci. 10 (2008) 651–658.
[26] T. Fujii, I. Terasaki, T. Watanabe, A. Matsuda, Jpn. J. Appl. Phys. 41 (2002) 783–786.
[27] T. Yamamoto, I. Tsukada, K. Uchinokura, M. Takagi, T. Tsubone, M. Ichihara, K. Kobayashi, Jpn. J. Appl. Phys. 39 (2000) 747–750.
[28] R. Funahashi, S. Urata, T. Sano, M. Kitawaki, J. Mater. Res. 18 (2003) 1646–16451.
[29] Y. Zhang, J. Zhang, Q. Lu, Ceram. Int. 33 (2007) 1305–1308.
[30] M. Mikami, E. Guilmeau, R. Funahashi, K. Chong, D. Chateigner, J. Mater. Res. 20 (2005) 2491–2497.
[31] V. Rouessac, G. Desgardin, M. Gomina, Phys. C 282–287 (1997) 2573–2574.